18. X.-G. Wang, T. Carrington Jr., *J. Chem. Phys.* **129**, 234102 (2008).
19. T. Oka, *J. Mol. Spectrosc.* **228**, 635–639 (2004).
20. Here *J* denotes the rotational quantum number comprising end-over-end rotation *R* and internal rotation.
21. P. Bunker, B. Ostojić, S. Yurchenko, *J. Mol. Struct.* **695–696**, 253 (2004).
22. Here we use the quantum number *J* instead of *R*, because the rotational motion in the state is not purely the end-over-end rotation.
23. M. Kolbuszewski, P. R. Bunker, *J. Chem. Phys.* **105**, 3649 (1996).
24. M. P. Deskevich, A. B. McCoy, J. M. Hutson, D. J. Nesbitt, *J. Chem. Phys.* **128**, 094306 (2008).

ACKNOWLEDGMENTS

We thank T. Carrington, P. Bunker, D. Nesbitt, P. Jensen, and U. Manthe for fruitful discussions on theoretical aspects of CH_5^+, as well as J. Krieg in the initial stage of the experiment. Supported by Deutsche Forschungsgemeinschaft grant SCHL 341/6-1. We gratefully acknowledge the support of the workshops of the I. Physikalisches Institut. The two line lists (for 10 K and 4 K) associated with Fig. 1 are available as supplementary material; the raw data are archived at the University of Cologne and are available upon request.

SUPPLEMENTARY MATERIALS

www.sciencemag.org/content/347/6228/1346/suppl/DC1
Materials and Methods
Tables S1 and S2
Reference (*25*)

21 November 2014; accepted 21 January 2015
10.1126/science.aaa3304

ADDITIVE MANUFACTURING

Continuous liquid interface production of 3D objects

John R. Tumbleston,[1] David Shirvanyants,[1] Nikita Ermoshkin,[1] Rima Janusziewicz,[2] Ashley R. Johnson,[3] David Kelly,[1] Kai Chen,[1] Robert Pinschmidt,[1] Jason P. Rolland,[1] Alexander Ermoshkin,[1]* Edward T. Samulski,[1,2]* Joseph M. DeSimone[1,2,4]*

Additive manufacturing processes such as 3D printing use time-consuming, stepwise layer-by-layer approaches to object fabrication. We demonstrate the continuous generation of monolithic polymeric parts up to tens of centimeters in size with feature resolution below 100 micrometers. Continuous liquid interface production is achieved with an oxygen-permeable window below the ultraviolet image projection plane, which creates a "dead zone" (persistent liquid interface) where photopolymerization is inhibited between the window and the polymerizing part. We delineate critical control parameters and show that complex solid parts can be drawn out of the resin at rates of hundreds of millimeters per hour. These print speeds allow parts to be produced in minutes instead of hours.

Additive manufacturing has become a useful technique in a wide variety of applications, including do-it-yourself 3D printing (*1*, *2*), tissue engineering (*3*–*5*), materials for energy (*6*, *7*), chemistry reactionware (*8*), molecular visualization (*9*, *10*), microfluidics (*11*), and low-density, high-strength materials (*12*–*15*). Current additive manufacturing methods such as fused deposition modeling, selective laser sintering, and stereolithography (*2*, *16*) are inordinately slow because they rely on layer-by-layer printing processes. A macroscopic object several centimeters in height can take hours to construct. For additive manufacturing to be viable in mass production, print speeds must increase by at least an order of magnitude while maintaining excellent part accuracy. Although oxygen inhibition of free radical polymerization is a widely encountered obstacle to photopolymerizing UV-curable resins in air, we show how controlled oxygen inhibition can be used to enable simpler and faster stereolithography.

Typically, oxygen inhibition leads to incomplete cure and surface tackiness when photopolymerization is conducted in air (*17*, *18*). Oxygen can either quench the photoexcited photoinitiator or create peroxides by combining with the free radical from the photocleaved photoinitiator (fig. S1). If these oxygen inhibition pathways can be avoided, efficient initiation and propagation of polymer chains will result. When stereolithography is conducted above an oxygen-permeable build window, continuous liquid interface production (CLIP) is enabled by creating an oxygen-containing "dead zone," a thin uncured liquid layer between the window and the cured part surface. We show that dead zone thicknesses on the order of tens of micrometers are maintained by judicious selection of control parameters (e.g., photon flux and resin optical and curing properties). Simple relationships describe the dead zone thickness and resin curing process, and, in turn, result in a straightforward relationship between print speed and part resolution. We demonstrate that CLIP can be applied to a range of part sizes from undercut micropaddles with stem diameters of 50 μm to complex handheld objects greater than 25 cm in size.

Figure 1A illustrates the simple architecture and operation of a 3D printer that takes advantage of an oxygen-inhibited dead zone. CLIP proceeds via projecting a continuous sequence of UV images (generated by a digital light-processing imaging unit) through an oxygen-permeable, UV-transparent window below a liquid resin bath. The dead zone created above the window maintains a liquid interface below the advancing part. Above the dead zone, the curing part is continuously drawn out of the resin bath, thereby creating suction forces that constantly renew reactive liquid resin. This nonstop process is fundamentally different from traditional bottom-up stereolithography printers, where UV exposure, resin renewal, and part movement must be conducted in separate and discrete steps (fig. S2). Even for inverted top-down approaches in which photopolymerization occurs at an air-resin interface [i.e., the part is successively lowered into a resin bath during printing (*16*, *19*)], these steps must be conducted sequentially for the formation of each layer. Because each step takes several seconds to implement for each layer, and because each layer of a part has a typical thickness of 50 to 100 μm, vertical print speeds are restricted to a few millimeters per hour (*16*). By contrast, the print speed for CLIP is limited by resin cure rates and viscosity (discussed below), not by stepwise layer formation. For example, the gyroid and argyle structures shown in Fig. 1B were printed at 500 mm/hour, reaching a height of ~5 cm in less than 10 min (movies S1 and S2). An additional benefit of a continual process is that the choice of 3D model slicing thickness, which affects part resolution, does not influence print speed, as shown in the ramp test patterns in Fig. 1C. Because CLIP is continuous, the refresh rate of projected images can be increased without altering print speed, ultimately allowing for smooth 3D objects with no model slicing artifacts.

Establishing an oxygen-inhibited dead zone is fundamental to the CLIP process. CLIP uses an amorphous fluoropolymer window (Teflon AF 2400) with excellent oxygen permeability (1000 barrers; 1 barrer = 10^{-10} cm^3(STP) cm cm^{-2} s^{-1} $cmHg^{-1}$) (*20*), UV transparency, and chemical inertness. Dead zone thickness measurements using a differential thickness technique (fig. S3) demonstrate the importance of both oxygen supply and oxygen permeability of the window in establishing the dead zone. Figure 2 shows that the dead zone thickness when pure oxygen is used below the window is about twice the thickness when air is used, with the dead zone becoming thinner as the incident photon flux increases (see below). When nitrogen is used below the window, the dead zone vanishes. A dead zone also does not form when Teflon AF 2400 is replaced by a material with very poor oxygen permeability, such as glass or polyethylene, even if oxygen is present below the window. Without a suitable dead zone, continuous part production is not possible.

For the case of ambient air below the window, Fig. 3A shows the dependence of dead zone thickness on incident photon flux (Φ_0), photoinitiator

[1]Carbon3D Inc., Redwood City, CA 94063, USA. [2]Department of Chemistry, University of North Carolina, Chapel Hill, NC 27599, USA. [3]Joint Department of Biomedical Engineering, University of North Carolina at Chapel Hill and North Carolina State University. [4]Department of Chemical and Biomolecular Engineering, North Carolina State University, Raleigh, NC 27695, USA.
*Corresponding author. E-mail: alex@carbon3d.com (A.E.); et@unc.edu (E.T.S.); desimone@email.unc.edu (J.M.D.)

Downloaded from http://science.sciencemag.org/ on March 16, 2019

Corrected 23 March 2015; see full text.

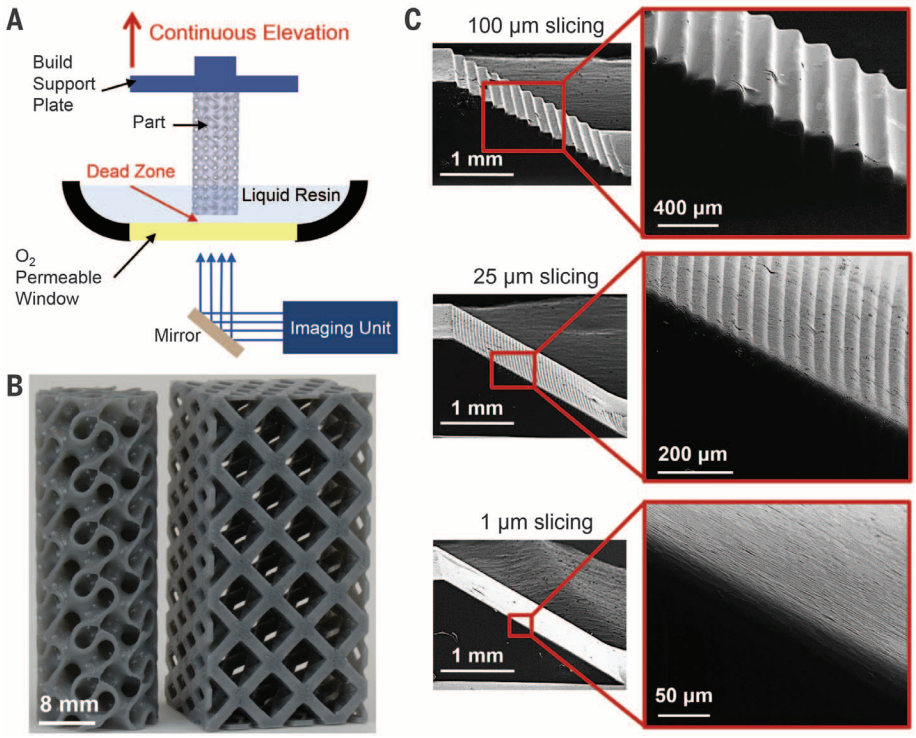

Fig. 1. CLIP enables fast print speeds and layerless part construction. (**A**) Schematic of CLIP printer where the part (gyroid) is produced continuously by simultaneously elevating the build support plate while changing the 2D cross-sectional UV images from the imaging unit. The oxygen-permeable window creates a dead zone (persistent liquid interface) between the elevating part and the window. (**B**) Resulting parts via CLIP, a gyroid (left) and an argyle (right), were elevated at print speeds of 500 mm/hour (movies S1 and S2). (**C**) Ramp test patterns produced at the same print speed regardless of 3D model slicing thickness (100 μm, 25 μm, and 1 μm).

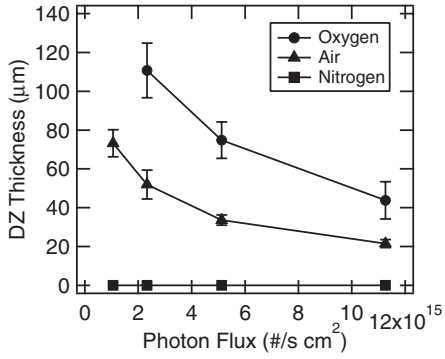

Fig. 2. The dead zone is created by oxygen permeation through the window. Dead zone thickness is shown as a function of incident photon flux. When pure oxygen is used below the gas-permeable window, the dead zone thickness increases. If nitrogen is used, the dead zone vanishes, resulting in adhesion of the cured resin to the window. Error bars represent SD of 10 measurements of the same conditions.

absorption coefficient (α_{PI}), and resin curing dosage (D_{c0}). These three control parameters are related to dead zone thickness according to

$$\text{Dead zone thickness} = C\left(\frac{\Phi_0 \alpha_{PI}}{D_{c0}}\right)^{-0.5} \quad (1)$$

where Φ_0 is the number of incident photons at the image plane per area per time, α_{PI} is the product of photoinitiator concentration and the wavelength-dependent absorptivity, D_{c0} quantifies the resin reactivity of a monomer-photoinitiator combination (fig. S4), and C is a proportionality constant. This relationship is similar to the one that describes photopolymerizable particle formation in microfluidic devices that use oxygen-permeable channel walls (*21*, *22*). The dead zone thickness behaves as follows: Increasing either Φ_0 or α_{PI} increases the concentration of free radicals in the resin (fig. S1) and decreases the initial oxygen concentration by reaction. Additional oxygen diffuses through the window and into the resin but decays with distance from the window, so that free radicals will overpower inhibiting oxygen at some distance from the window. At the threshold distance where all oxygen is consumed and free radicals still exist, polymerization will begin. Increasing the reactivity of the resin (i.e., decreasing D_{c0}) causes the polymerization threshold distance from the window to also shrink, thus making the dead zone thinner. The proportionality constant C in Eq. 1 has a value of ~30 for our case of 100-μm-thick Teflon AF 2400 with air below the window, and has units of the square root of diffusivity. The flux of oxygen through the window is also important in maintaining a stable dead zone over time, which is commonly described in terms of the ratio of film permeability to film thickness (*23*). Using these relationships enables careful control of the dead zone, which provides a critical resin renewal layer between the window and the advancing part.

Above the dead zone, photopolymerization occurs to a certain cured thickness that depends on $\Phi_0\alpha_{PI}/D_{c0}$ along with exposure time (t) and the resin absorption coefficient (α) according to the relationship

$$\text{Cured thickness} = \frac{1}{\alpha}\ln\left(\frac{\Phi_0 \alpha_{PI} t}{D_{c0}}\right) \quad (2)$$

Figure 3B shows cured thickness for three different resins with varying α (holding α_{PI} constant) where thicknesses were measured for different UV photon dosages (products of Φ_0 and t) (fig. S3). These curves are akin to the so-called "working curves" used in stereolithography resin characterization (*16*, *19*). For these resins, α is varied by adjusting the concentration of an absorbing dye or pigment that passively absorbs light (i.e., does not produce radicals) but contributes to overall resin absorption via $\alpha = \alpha_{PI} + \alpha_{dye}$. Note that α is the inverse of the characteristic optical absorption height (h_A) of the resin:

$$h_A = \frac{1}{\alpha} \quad (3)$$

The value of h_A, in conjunction with the model slicing thickness (Fig. 1C), projected pixel size, and image quality, determines the part resolution. The projected pixel size (typically between 10 and 100 μm) and image quality are functions of the imaging setup and determine lateral part resolution. As with slicing thickness, h_A affects vertical resolution but is a property of the resin. If h_A is high, then previously cured 2D patterns will continue to be exposed, causing unintentional overcuring and "print-through," which in turn results in defects for undercut and overhang geometries.

From the expressions for dead zone thickness and cured thickness, a simple relationship among print speed, h_A (i.e., resolution), and $\Phi_0\alpha_{PI}/D_{c0}$ is derived:

$$\frac{\text{Speed}}{h_A} \propto \frac{\Phi_0 \alpha_{PI}}{D_{c0}} \quad (4)$$

(see supplementary materials). Figure 3C shows a contour plot of speed as a function of h_A and the ratio $\Phi_0\alpha_{PI}/D_{c0}$; the dead zone thickness (Eq. 1) is indicated. For a given h_A, speed can be increased by increasing Φ_0 or α_{PI} or by using a resin with lower D_{c0}. However, as speed increases, dead zone thickness decreases and will eventually become too thin for the process to remain stable. For CLIP, the empirically determined minimum dead zone thickness is ~20 to 30 μm. Part production with a dead zone thickness below this minimum is possible but can lead to window adhesion–related defects. Once the minimum dead zone thickness is reached, the print speed can only be increased by relaxing the resolution (i.e., using a resin with higher h_A).

Downloaded from http://science.sciencemag.org/ on March 16, 2019

Corrected 23 March 2015; see full text.

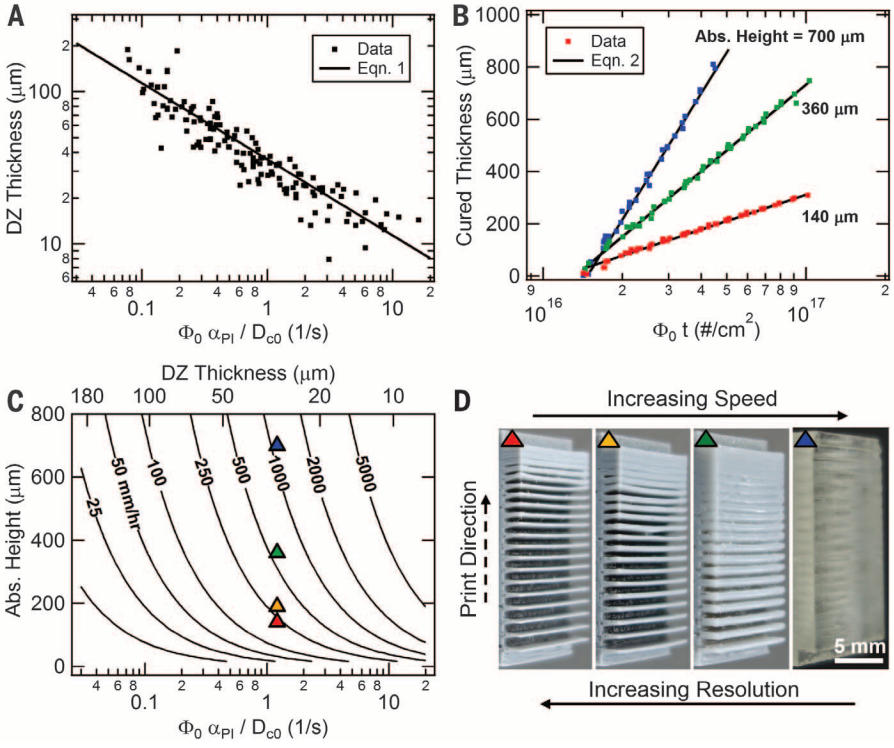

Fig. 3. A trade off exists between print speed and part resolution. (**A**) Liquid interface dead zone (DZ) thickness as a function of $\Phi_0\alpha_{PI}/D_{c0}$. These parameters have typical ranges: 5×10^{14} cm^{-2} s^{-1} < Φ_0 < 2×10^{16} cm^{-2} s^{-1}; 2×10^{-4} μm^{-1} < α_{PI} < 1×10^{-2} μm^{-1}; 5×10^{12} cm^{-2} μm^{-1} < D_{c0} < 5×10^{13} cm^{-2} μm^{-1}. (**B**) Cured thickness as a function of UV photon dosage ($\Phi_0 t$) for three resins with different h_A controlled with dye loading. (**C**) CLIP print speed contours as functions of h_A and $\Phi_0\alpha_{PI}/D_{c0}$. (**D**) Photographs of resolution test patterns using resins with different h_A from (B). Colored triangles correspond to process conditions in (C). The dye-free test pattern produced at highest print speed (blue triangle) is semitransparent.

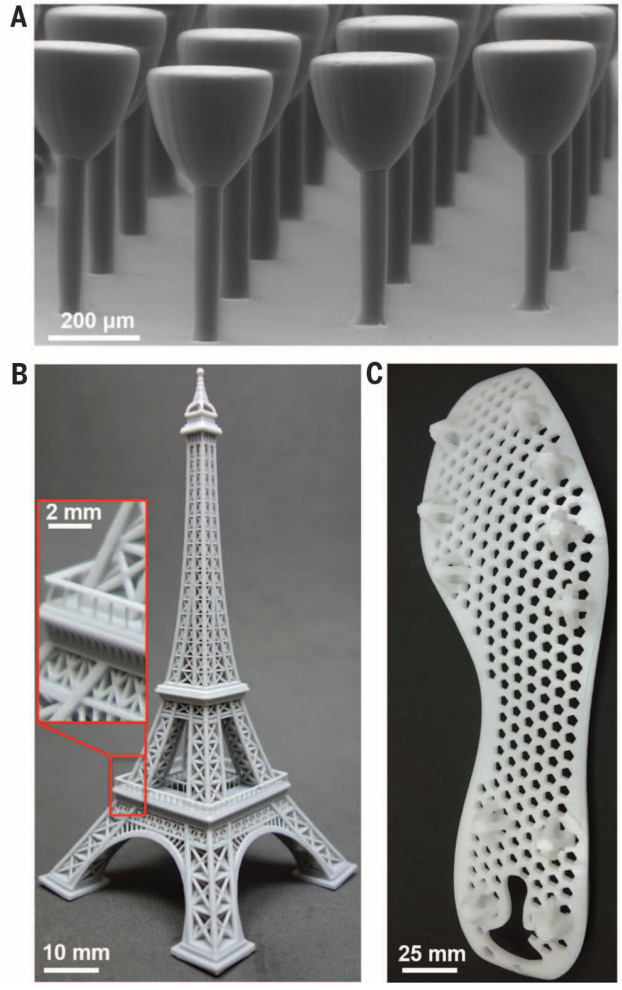

Fig. 4. A variety of parts can be fabricated using CLIP. (**A**) Micropaddles with stems 50 μm in diameter. (**B**) Eiffel Tower model, 10 cm tall. (**C**) A shoe cleat >20 cm in length. Even in large parts, fine detail is achieved, as shown in the inset of (B) where features <1 mm in size are obtained. The micropaddles were printed at 25 mm/hour; the Eiffel Tower model and shoe cleat were printed at 100 mm/hour.

This analysis shows that for a dead zone thickness of 20 μm, speeds in excess of 300 mm/hour with h_A = 100 μm are accessible. By increasing h_A to 300 μm and sacrificing resolution, speeds greater than 1000 mm/hour are readily achieved. The trade off between speed and resolution is demonstrated in Fig. 3D with resolution test patterns using the resins with different h_A from Fig. 3B (all have equivalent $\Phi_0\alpha_{PI}/D_{c0}$ and dead zone thickness). As dye loading is increased, h_A is reduced, leading to less print-through and ultimately higher resolution. However, dye absorption does not produce free radicals, so resins with lower h_A require greater dosages to adequately solidify; that is, parts must be elevated more slowly for constant photon flux. On the other hand, the resin without dye and with the highest h_A can be printed at the greatest speed but with poor resolution (as shown by unintentional curing of the overhangs in the test pattern).

Using this process control framework, Fig. 4 shows an array of expediently produced parts ranging in size from undercut micropaddles with stem diameters of 50 μm (Fig. 4A) to full-size shoe cleats 25 cm in length (Fig. 4C). The Eiffel Tower model in Fig. 4B illustrates that fine detail is achieved even in macroscale parts: The horizontal railing posts (diameter <500 μm) are resolved on this 10-cm-tall model. This ratio of scales (1:200) confirms that the CLIP process enables rapid production of arbitrary microscopic features over parts having macroscopic dimensions. For these parts, the speed-limiting process is resin curing (Eq. 4); however, for other part geometries, the speed-limiting process is resin flow into the build area. For such geometries with comparatively wide solid cross sections, parameters that affect

Downloaded from http://science.sciencemag.org/ on March 16, 2019

Corrected 23 March 2015; see full text.

resin flow (e.g., resin viscosity, suction pressure gradient) become important to optimize.

Preliminary studies show that the CLIP process is compatible with producing parts from soft elastic materials (*24*, *25*), ceramics (*26*), and biological materials (*27*, *28*). CLIP has the potential to extend the utility of additive manufacturing to many areas of science and technology, and to lower the manufacturing costs of complex polymer-based objects.

REFERENCES AND NOTES

1. J. M. Pearce, *Science* **337**, 1303–1304 (2012).
2. H. Lipson, M. Kurman, *Fabricated: The New World of 3D Printing* (Wiley, Indianapolis, 2013).
3. B. Derby, *Science* **338**, 921–926 (2012).
4. A. Atala, F. K. Kasper, A. G. Mikos, *Sci. Transl. Med.* **4**, 160rv12 (2012).
5. B. C. Gross, J. L. Erkal, S. Y. Lockwood, C. Chen, D. M. Spence, *Anal. Chem.* **86**, 3240–3253 (2014).
6. K. Sun *et al.*, *Adv. Mater.* **25**, 4539–4543 (2013).
7. G. Chisholm, P. J. Kitson, N. D. Kirkaldy, L. G. Bloor, L. Cronin, *Energy Environ. Sci.* **7**, 3026–3032 (2014).
8. M. D. Symes *et al.*, *Nat. Chem.* **4**, 349–354 (2012).
9. P. Chakraborty, R. N. Zuckermann, *Proc. Natl. Acad. Sci. U.S.A.* **110**, 13368–13373 (2013).
10. P. J. Kitson *et al.*, *Cryst. Growth Des.* **14**, 2720–2724 (2014).
11. J. L. Erkal *et al.*, *Lab Chip* **14**, 2023–2032 (2014).
12. X. Zheng *et al.*, *Science* **344**, 1373–1377 (2014).
13. T. A. Schaedler *et al.*, *Science* **334**, 962–965 (2011).
14. J. Bauer, S. Hengsbach, I. Tesari, R. Schwaiger, O. Kraft, *Proc. Natl. Acad. Sci. U.S.A.* **111**, 2453–2458 (2014).
15. E. B. Duoss *et al.*, *Adv. Funct. Mater.* **24**, 4905–4913 (2014).
16. I. Gibson, D. W. Rosen, B. Stucker, *Additive Manufacturing Technologies: Rapid Prototyping to Direct Digital Manufacturing* (Springer, New York, 2010).
17. S. C. Ligon, B. Husár, H. Wutzel, R. Holman, R. Liska, *Chem. Rev.* **114**, 557–589 (2014).
18. Y. Yagci, S. Jockusch, N. J. Turro, *Macromolecules* **43**, 6245–6260 (2010).
19. P. F. Jacobs, *Rapid Prototyping & Manufacturing: Fundamentals of StereoLithography* (Society of Manufacturing Engineers, Dearborn, MI, 1992).
20. T. C. Merkel, I. Pinnau, R. Prabhakar, B. D. Freeman, *Materials Science of Membranes for Gas and Vapor Separation* (Wiley, West Sussex, UK, 2006), pp. 251–270.
21. D. Dendukuri *et al.*, *Macromolecules* **41**, 8547–8556 (2008).
22. D. Dendukuri, D. C. Pregibon, J. Collins, T. A. Hatton, P. S. Doyle, *Nat. Mater.* **5**, 365–369 (2006).
23. J. M. Gonzalez-Meijome, V. Compañ-Moreno, E. Riande, *Ind. Eng. Chem. Res.* **47**, 3619–3629 (2008).
24. J. A. Rogers, T. Someya, Y. Huang, *Science* **327**, 1603–1607 (2010).
25. S. Bauer *et al.*, *Adv. Mater.* **26**, 149–161 (2014).
26. N. Travitzky *et al.*, *Adv. Eng. Mater.* **16**, 729–754 (2014).
27. C. Cvetkovic *et al.*, *Proc. Natl. Acad. Sci. U.S.A.* **111**, 10125–10130 (2014).
28. Y. Lu, G. Mapili, G. Suhali, S. Chen, K. Roy, *J. Biomed. Mater. Res. A* **77**, 396–405 (2006).

ACKNOWLEDGMENTS

This work was sponsored by Carbon3D Inc. J.R.T., D.S., N.E., D.K., R.P., J.P.R., A.E., E.T.S., and J.M.D. all have an equity stake in Carbon3D Inc., which is a venture-backed startup company. Continuous liquid interface printing is the subject of patent protection including Patent Cooperation Treaty publication numbers WO 2014/126837 A2, WO 2014/126830 A2, and WO 2014/126834 A2, and others.

SUPPLEMENTARY MATERIALS

www.sciencemag.org/content/347/6228/1349/suppl/DC1
Materials and Methods
Supplementary Text
Figs. S1 to S4
Movies S1 and S2
Reference (*29*)

5 November 2014; accepted 3 February 2015
10.1126/science.aaa2397

PALEOANTHROPOLOGY

Early *Homo* at 2.8 Ma from Ledi-Geraru, Afar, Ethiopia

Brian Villmoare,[1,4,6]* William H. Kimbel,[2]* Chalachew Seyoum,[2,7] Christopher J. Campisano,[2] Erin N. DiMaggio,[3] John Rowan,[2] David R. Braun,[4] J Ramón Arrowsmith,[5] Kaye E. Reed[2]

Our understanding of the origin of the genus *Homo* has been hampered by a limited fossil record in eastern Africa between 2.0 and 3.0 million years ago (Ma). Here we report the discovery of a partial hominin mandible with teeth from the Ledi-Geraru research area, Afar Regional State, Ethiopia, that establishes the presence of *Homo* at 2.80 to 2.75 Ma. This specimen combines primitive traits seen in early *Australopithecus* with derived morphology observed in later *Homo*, confirming that dentognathic departures from the australopith pattern occurred early in the *Homo* lineage. The Ledi-Geraru discovery has implications for hypotheses about the timing and place of origin of the genus *Homo*.

Fifty years after the recognition of the species *Homo habilis* as the earliest known representative of our genus (*1*), the origin of *Homo* remains clouded. This uncertainty stems in large part from a limited fossil record between 2.0 and 3.0 million years ago (Ma), especially in eastern Africa. Some taxa from this time period, such as *Australopithecus africanus* (~2.8 to 2.3 Ma) and the less well known *A. garhi* (~2.5 Ma) and *A. aethiopicus* (~2.7 to 2.3 Ma), appear too specialized cranially and/or dentally to represent the probable proximate ancestral conditions for *Homo* species known in Africa by ~2.0 Ma (*H. habilis* and *H. rudolfensis*). This leaves a thin scatter of isolated, variably informative specimens dated to 2.4 to 2.3 Ma as the only credible fossil evidence bearing on the earliest known populations of the genus *Homo* (*2*, *3*).

Here we describe a recently recovered partial hominin mandible, LD 350-1, from the Ledi-Geraru research area, Afar Regional State, Ethiopia, that extends the fossil record of *Homo* back in time a further 0.4 million years. The specimen, securely dated to 2.80 to 2.75 Ma, combines derived morphology observed in later *Homo* with primitive traits seen in early *Australopithecus*. The discovery has implications for hypotheses concerning the timing and place of *Homo* origins.

The LD 350 locality resides in the Lee Adoyta region of the Ledi-Geraru research area (Fig. 1). Geologic research at Lee Adoyta (*4*) identified fault-bounded sedimentary packages dated 2.84 to 2.58 Ma. The LD 350-1 mandible was recovered on the surface of finely bedded fossiliferous silts 10 m conformably above the Gurumaha Tuff (Fig. 1). The matrix adherent to the specimen is consistent with it having eroded from these silts [for details on stratigraphy and depositional environment, see (*4*)]. The Gurumaha Tuff is radiometrically dated to 2.822 ± 0.006 Ma (*4*), a date that is consistent with the normal magnetic polarity of the Gurumaha section, presumably the Gauss Chron. An upper bounding age for LD 350-1 is provided by an adjacent downfaulted younger block that contains the 2.669 ± 0.011 Ma Lee Adoyta Tuff. A magnetostratigraphic reversal 12 m conformably above the Lee Adoyta Tuff is inferred to be the Gauss/Matuyama boundary at 2.58 Ma (*4*). Because no significant erosional events intervene between the Gurumaha Tuff and the fossiliferous horizon, the age of LD 350-1 can be further constrained by stratigraphic scaling. Applying a sedimentation rate of either 14 cm per thousand years (ky) from the Lee Adoyta fault block or 30 cm/ky from the Hadar Formation (*5*) provides age estimates of 2.77 and 2.80 million years (My), respectively, for LD 350-1. Based on the current chronostratigraphic framework for Ledi-Geraru, we consider the age of LD 350-1 to be 2.80 to 2.75 My.

The hominin specimen, found by Chalachew Seyoum on 29 January 2013, comprises the left side of an adult mandibular corpus that preserves the partial or complete crowns and roots of the canine, both premolars, and all three molars. The corpus is well preserved from the symphysis to the root of the ascending ramus and retromolar platform. Surface detail is very good to excellent, and there is no evidence of significant transport. The inferior margin of the corpus and the lingual alveolar margin are intact, but the buccal alveolar margin is chipped between P_3 and M_1. The P_4, M_2, and M_3 crowns are complete and well preserved, but the C, P_3, and M_1 crowns are incomplete (Fig. 2 and text S2). The anterior dentition is represented by the broken root of the lateral incisor and the alveolus of the central incisor.

Given its location and age, it is natural to ask whether the LD 350-1 mandible represents a late-surviving population of *A. afarensis*, whose

[1]Department of Anthropology, University of Nevada Las Vegas, Las Vegas, NV 89154, USA. [2]Institute of Human Origins and School of Human Evolution and Social Change, Arizona State University, Tempe, AZ 85287, USA. [3]Department of Geosciences, Pennsylvania State University, University Park, PA 16802, USA. [4]Center for the Advanced Study of Hominin Paleobiology, George Washington University, Washington, DC 20052, USA. [5]School of Earth and Space Exploration, Arizona State University, Tempe, AZ 85281, USA. [6]Department of Anthropology, University College London, London WC1H 0BW, UK. [7]Authority for Research and Conservation of Cultural Heritage, Addis Ababa, Ethiopia.
***Corresponding author. E-mail: brian.villmoare@unlv.edu (B.V.); wkimbel.iho@asu.edu (W.H.K.)**

Downloaded from http://science.sciencemag.org/ on March 16, 2019

Corrected 23 March 2015; see full text.

Science

Continuous liquid interface production of 3D objects

John R. Tumbleston, David Shirvanyants, Nikita Ermoshkin, Rima Janusziewicz, Ashley R. Johnson, David Kelly, Kai Chen, Robert Pinschmidt, Jason P. Rolland, Alexander Ermoshkin, Edward T. Samulski and Joseph M. DeSimone

Science **347** (6228), 1349-1352.
DOI: 10.1126/science.aaa2397originally published online March 16, 2015

Fast, continuous, 3D printing

Although three-dimensional (3D) printing is now possible using relatively small and low-cost machines, it is still a fairly slow process. This is because 3D printers require a series of steps to cure, replenish, and reposition themselves for each additive cycle. Tumbleston *et al.* devised a process to effectively grow solid structures out of a liquid bath. The key to the process is the creation of an oxygen-containing "dead zone" between the solid part and the liquid precursor where solidification cannot occur. The precursor liquid is then renewed by the upward movement of the growing solid part. This approach made structures tens of centimeters in size that could contain features with a resolution below 100 μm.

Science, this issue p. 1349

ARTICLE TOOLS http://science.sciencemag.org/content/347/6228/1349

SUPPLEMENTARY MATERIALS http://science.sciencemag.org/content/suppl/2015/03/16/science.aaa2397.DC1

REFERENCES This article cites 25 articles, 9 of which you can access for free
http://science.sciencemag.org/content/347/6228/1349#BIBL

PERMISSIONS http://www.sciencemag.org/help/reprints-and-permissions

Use of this article is subject to the Terms of Service

Science (print ISSN 0036-8075; online ISSN 1095-9203) is published by the American Association for the Advancement of Science, 1200 New York Avenue NW, Washington, DC 20005. 2017 © The Authors, some rights reserved; exclusive licensee American Association for the Advancement of Science. No claim to original U.S. Government Works. The title *Science* is a registered trademark of AAAS.

Downloaded from http://science.sciencemag.org/ on March 16, 2019